Analysis of 10.7-μm Brightness Temperatures of a Simulated Thunderstorm with Two-Moment Microphysics

LEWIS D. GRASSO AND THOMAS J. GREENWALD

Cooperative Institute for Research in the Atmosphere, Fort Collins, Colorado

(Manuscript received 13 December 2002, in final form 23 September 2003)

ABSTRACT

A cloud-resolving model was used in conjunction with a radiative transfer (RT) modeling system to study 10.7-μm brightness temperatures computed for a simulated thunderstorm. A two-moment microphysical scheme was used that included seven hydrometeor types: pristine ice, snow, aggregates, graupel, hail, rain, and cloud water. Also, five different habits were modeled for pristine ice and snow. Hydrometeor optical properties were determined from an extended anomalous diffraction theory approach. Brightness temperatures were computed using a delta-Eddington two-stream model.

Results indicate that the enhanced ''V,'' a feature sometimes seen in satellite infrared observations, may be formed through an interaction between the overshooting dome and the upstream flanking region of high pressure. This idea is contrary to one in which the overshooting dome is viewed as an obstacle to the environmental flow. As expected, the radiative effects of pristine ice particles within the anvil largely determined the brightness temperature field. Although brightness temperatures were found to be insensitive to microphysical characteristics of moderate to thick portions of the anvil, a strong relationship did exist with column-integrated pristine ice mass for cloud optical depths below about 5. Precipitation-sized hydrometeors and surface precipitation rate, on the other hand, failed to exhibit any meaningful relationship with the cloud-top brightness temperature. The combined mesoscale model and RT modeling system used in this study may also have utility in satellite product development prior to launch of a satellite and in satellite data assimilation.

1. Introduction

Observations in the 10.7-μm infrared window have proven useful for studying the cloud-top behavior and intensity of thunderstorms, including the enhanced ''V'' signature (e.g., Heymsfield and Blackmer 1988; Adler et al. 1983; McCann 1983; Adler and Fenn 1979). These observations, conjoined with other ancillary data, have also had use in estimating rainfall rates for operational purposes (Vicente et al. 1998) and for global climate studies (Huffman et al. 1997). However, simulated 10.7-μm brightness temperatures (T_bs) may provide benefit in interpreting observations of thunderstorms. For example, operational numerical models with the capability of producing synthetic infrared imagery may provide another useful tool for severe weather forecasters. In addition, techniques to rapidly compute infrared T_bs in cloudy regions are of current interest in data assimilation research (Greenwald et al. 2002).

Despite the importance of simulating infrared T_bs using modeled cloud fields, a relative dearth of information on this topic exists in the literature. Recently, Greenwald et al. (2002) developed a general-purpose observational operator—a system that transforms model state variables into radiance—for use at visible and infrared wavelengths in both clear-sky and cloudy regions. Limited results for a continental stratus system indicated that simulated cloudy radiances compared favorably to Geostationary Operational Environmental Satellite (GOES) imager observations. Chevallier et al. (2001) and Chevallier and Kelly (2002) also compared simulated infrared and microwave T_bs to satellite observations in preparation for global-scale operational assimilation of cloudy satellite radiances.

This study extends the work of Greenwald et al. (2002) to a simulated severe thunderstorm in order to examine the general characteristics of simulated GOES imager 10.7-μm T_bs and to gain further insight into the physical processes that create the enhanced V. Three new aspects of this research are 1) a prognostic two-moment microphysical scheme; 2) calculation of hydrometeor optical properties using physical models, rather than lookup tables or empirical methods; and 3) a practical means of computing infrared T_bs that includes multiple scattering effects for highly optically thick clouds containing many different types of hydrometeors.

This paper is divided into five sections. Brief descriptions of the numerical model used for the thun-

Corresponding author address: Dr. Lewis D. Grasso, NOAA/NESDIS/RAMMT CIRA, Colorado State University, West Laporte Avenue, Fort Collins, CO 80523.
E-mail: grasso@genesis.cira.colostate.edu

derstorm simulation and the radiative transfer modeling appear in section 2. Section 3 describes the simulated T_b fields and includes a discussion of the enhanced V. Relationships between T_bs and the storm microphysics are found in section 4. The conclusions and future developments round out the paper.

2. Numerical procedures

The numerical cloud model used for this study was the Regional Atmospheric Modeling System (RAMS), version 4.29, developed at Colorado State University (Pielke et al. 1992). The following features of RAMS were used to simulate the thunderstorm:

- The model was run nonhydrostatically and compressible (Tripoli and Cotton 1982).
- Momentum was advanced using a leapfrog scheme, while scalars were advanced using a forward scheme; in addition, both methods used second-order advection.
- Vertical and horizontal turbulence coefficients were parameterized using the Smagorinsky (1963) deformation-based eddy viscosity with stability modifications (Lilly 1962).
- Hydrometeors were predicted with a two-moment bulk microphysical scheme (Meyers et al. 1997). Mass mixing ratio and number concentration were prognosed for six of the seven hydrometeor types while the mean diameter was diagnosed. Cloud droplet mass mixing ratio, however, was predicted using a one-moment scheme. Work is ongoing to include cloud droplets into the two-moment scheme. The following hydrometeor species were included in the simulation: cloud droplets, rain droplets, aggregates, graupel, hail, snow, and pristine ice. Both graupel and hail are mixed phased; that is, liquid water may exist on the surface of the two particles. However, in computing optical properties, both graupel and hail were assumed to be homogeneous. Snow and pristine ice are each divided into five habit categories: columns, hexagonal, dendritic, needles, and rosetta.
- Other prognostic variables were the three components of velocity—u, v, w; perturbation Exner function, π^*; total water, r_t; and ice–liquid potential temperature, θ_{il} (Tripoli and Cotton 1981).
- RAMS uses the Arakawa fully staggered C grid (Arakawa and Lamb 1981).
- Perturbation Exner function tendencies, used to update the momentum variables, were computed using a time-split scheme—similar to Klemp and Wilhelmson (1978).
- Lateral boundaries used the Klemp–Wilhelmson condition; that is, the normal velocity component specified at the lateral boundary is effectively advected from the interior.
- A wall, with friction layers, was specified at the top boundary.

Two grids were initialized horizontally homogeneously while a warm bubble was used to trigger convection. Horizontal grid spacings of 4 km—approximately equal to the footprint of *GOES-9* 10.7-μm imager—were used within a domain spanning 400 km $\times$ 400 km. A nested grid—spanning 80 km in each horizontal direction—was used to improve the resolution of the simulated convective updraft and had horizontal grid spacings of 2 km. The domain of both grids extended to a height of approximately 23 km. Vertical grid spacings started at 100 m at the lower boundary and were stretched by a factor of 1.1 to a value of 2000 m. A time step of 5 s was used, and the simulation spanned 2 h. Initialization of the domain was similar to that of Grasso (2000). The sounding used to initialize both grids was retrieved from the *GOES-11* sounder at 2146 UTC 24 July 2000 near 41°N, 99.5°W: south-central Nebraska. Wind profilers from Neligh and McCook, Nebraska, were used to initialize the winds within the domain.

The observational operator used for computing brightness temperatures was developed at the Cooperative Institute for Research in the Atmosphere (Greenwald et al. 2002). It consists of three main components: radiative transfer models, hydrometeor optical (or single scatter) property models, and a gas extinction model. The specific components are the following:

- Radiative transfer model at solar wavelengths: Spherical harmonic discrete ordinate method (SHDOM; Evans 1998).
- Radiative transfer model at infrared wavelengths: Delta-Eddington two-stream method (Deeter and Evans 1998).
- Cloud optical property models at all wavelengths: Based on anomalous diffraction theory (Mitchell 2000; Mitchell 2002; Greenwald et al. 2002) applied to both liquid and ice particles.
- Gas extinction model at all wavelengths: Optical path transmittance (OPTRAN; McMillin et al. 1995a,b).

OPTRAN provides the gas optical depth between each level in the RAMS given profiles of temperatures, water vapor mixing ratio, pressure, and ozone (ppmv). The *U.S. Standard Atmosphere, 1976* profile for ozone was used. The lower boundary conditions for the delta-Eddington two-stream model were set as 0.98 for the surface emissivity; the simulated RAMS air temperature at the lowest model level was used as the surface temperature. Because of our interest in cloudy radiances, precise values of these boundary conditions are not crucial.

In this study, key parts of the operator are those that transform microphysical variables from RAMS into optical (single scatter) properties. Anomalous diffraction theory (ADT) is used to estimate all three properties: extinction coefficient, single-scattering albedo, and asymmetry factor for a distribution of particles (see Greenwald et al. 2002). Since RAMS is limited to pre-

diction of mixing ratio and number concentration, a gamma distribution of particles was assumed (Greenwald et al. 2002). In addition, the number concentration of cloud liquid water is set to 10^7 kg^{-1}. The width parameter ν in the gamma distribution is set to 1 for all hydrometeors since this parameter has little influence on scattering properties at 10.7 μm.

To extend ADT to different particle shapes, Mitchell (2002) incorporates mass- and area-dimensional relationships

$$m = \alpha D^{\beta}, \tag{1}$$

$$A = \gamma D^{\sigma}, \tag{2}$$

where D is particle diameter, m is mass, and A is projected area. Values of α, β, γ, and σ for different particle types are obtained from Mitchell (1996). Thus, the mean particle diameter of the gamma distribution becomes

$$\overline{D} = (\nu + 1)\left[\frac{\Gamma(\nu + 1)r_c}{\alpha\Gamma(\beta + \nu + 1)N_c}\right]^{1/\beta}, \tag{3}$$

where r_c and N_c are mixing ratio and number concentration, respectively, and Γ is the gamma function. Other than particle mixing ratio and number concentration, ADT also requires wavelength of radiation, bulk particle density, and particle refractive index. The density of hail is set to 0.9 g cm^{-3} while all other ice hydrometeors have a density of 0.8 g cm^{-3}. Liquid water was assigned a density of 1 g cm^{-3}. Complex refractive indices of water and ice at 10.7 μm are $1.1707 + 0.0798i$ and $1.0955 + 0.1516i$, respectively (Downing and Williams 1975; Warren 1984).

Effective optical properties of a mixture of different hydrometeor types are computed as follows (Mitchell and Arnott 1994):

$$\beta_{\text{ext,eff}} = \frac{1}{N_t}\sum_{i=1}^{n} \beta_{\text{ext},i}N_i, \tag{4}$$

$$\omega_{\text{eff}} = \frac{1}{N_t}\sum_{i=1}^{n} \omega_i N_i, \tag{5}$$

$$g_{\text{eff}} = \frac{1}{N_t}\sum_{i=1}^{n} g_i N_i, \tag{6}$$

where $N_t = \Sigma_{i=1}^{n} N_i$, the total number concentration of all hydrometeors. In the above equations, $\beta_{\text{ext},i}$, ω_i, g_i, and N_i represent the extinction, single-scatter albedo, asymmetry factor, and number concentration of the ith hydrometeor type. Further modification of ω_{eff} is required to account for gas extinction:

$$\omega^*_{\text{eff}} = \frac{\omega_{\text{eff}}\beta_{\text{ext,eff}}}{\beta_{\text{ext},t}}, \tag{7}$$

where $\beta_{\text{ext},t} = \beta_{\text{ext,eff}} + \beta_{\text{gas}}$.

Additional diagnostic quantities were computed to aid in the analysis. These included the column-integrated mass mixing ratio (CIRx), the weighting function (WFRx), and effective mean particle diameter (EFFDRx). The ''x'' in each acronym is replaced by either a (aggregates), c (cloud liquid water), g (graupel), h (hail), p (pristine ice), r (rain), or s (snow). Column-integrated mass mixing ratio is

$$\text{CIRx} = \int_0^{Z_{\text{top}}} R_x\rho\, dz, \tag{8}$$

where R_x is the mixing ratio of a given hydrometeor type. The weighting function is defined here as

$$\text{WFRx}(Z) = \left\{1 + (1 + \epsilon)\left[\frac{T(Z_s)}{T(Z)}\right]^2\right\}\frac{\partial T(Z)}{\partial Z}, \tag{9}$$

where ϵ is surface emissivity, $T(Z_s)$ represents the transmittance from the surface of the earth to the satellite, while $T(Z)$ is the transmittance from Z to the satellite (Liou 1980). Last, the effective mean diameter was computed as

$$\text{EFFDRx} = \frac{\displaystyle\int_0^{Z_{\text{top}}} \text{WFRx}\overline{D}\, dz}{\displaystyle\int_0^{Z_{\text{top}}} \text{WFRx}\, dz}. \tag{10}$$

3. Brightness temperature characteristics

A warm bubble was used to initiate the thunderstorm in the northwest corner of the domain. After precipitation reached the surface, the updraft moved southward to the right of the mean tropospheric northwesterly flow. Because of evaporation of precipitation, a cold pool expanded horizontally to the northwest along the surface. At 2 h into the simulation the anvil had expanded significantly and occupied a relatively large area. This is illustrated in the simulated *GOES-9* imager 10.7-μm T_b field computed at a zenith angle of 40° (Fig. 1a). The actual physical extent of the anvil, however, was even much greater as shown by the CIRp field (Fig. 1b).

Features typical of some observed thunderstorms were reproduced in the simulation. For example, the location of the convective updraft, or overshooting dome, occurred as a localized minimum of T_bs ($x = 168$ km and $y = 220$ km) near the vertex of the enhanced V. The enhanced V itself was several degrees colder than the T_b of the surrounding anvil. Near the center of the anvil was a localized warm region. Within the thickest parts of the anvil, T_bs varied about 10 K.

One way to help interpret the T_b field is through the concept of a weighting function. This function identifies at what levels in the atmosphere the radiation originates. Figure 2 shows two different vertical cross sections of the total weighting function, that is, the combined effects of all hydrometeors, taken through the overshooting dome and through the body of the anvil (refer to Fig. 1a). The main feature is that the weighting function

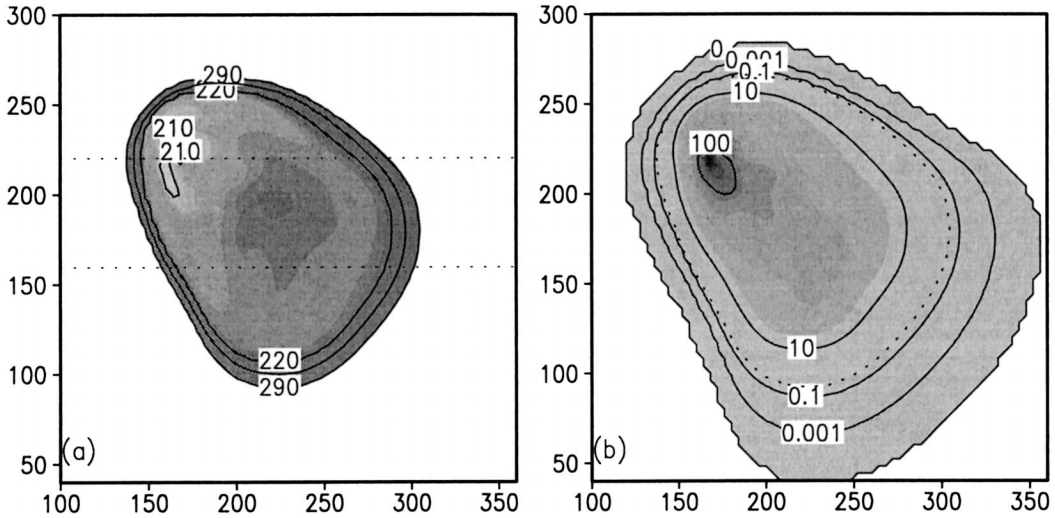

FIG. 1. Shaded and contoured values of (a) 10.7-μm T_bs (K) and (b) column-integrated pristine ice (kg m^{-2}; multiplied by 100). Horizontal dotted contours in (a) depict the location of vertical cross sections for Fig. 2. The dotted contour in (b) is the 290-K brightness temperature. In this plot and all others, both the horizontal and vertical axes are in km. Lighter/darker shades represent smaller/greater values of plotted variables in all figures. All plots are at 7200 s.

peaks in the upper regions of the anvil, essentially near the cloud top. Also, because of the vertical transport of significant cloud material by the main updraft, the weighting function bends upward a few kilometers above the environmental equilibrium level at approximately 15 km. The downward bending of the weighting function near the anvil edges is a result of very small optical depths. Comparing the simulated environmental temperature field (also included in Fig. 2) to the T_b field in Fig. 1 shows that the radiation originates at levels slightly below the maximum values of the weighting function. The cause of this behavior is not clear, but may be due to warm biases in the delta-Eddington two-stream model, which may reach 1–2 K in highly optically thick conditions.

Results also indicated that the total weighting function was essentially dominated by the weighting function for pristine ice. Consequently, neglecting all hydrometeors except pristine ice in the radiative transfer calculations was sufficient to accurately reproduce the T_b field. There were, however, brightness temperature errors of a few degrees along the forward, southern edge of the anvil due to the neglect of the radiative effects of snow.

To aid in further analysis of the enhanced V, horizontal wind vector and perturbation Exner function

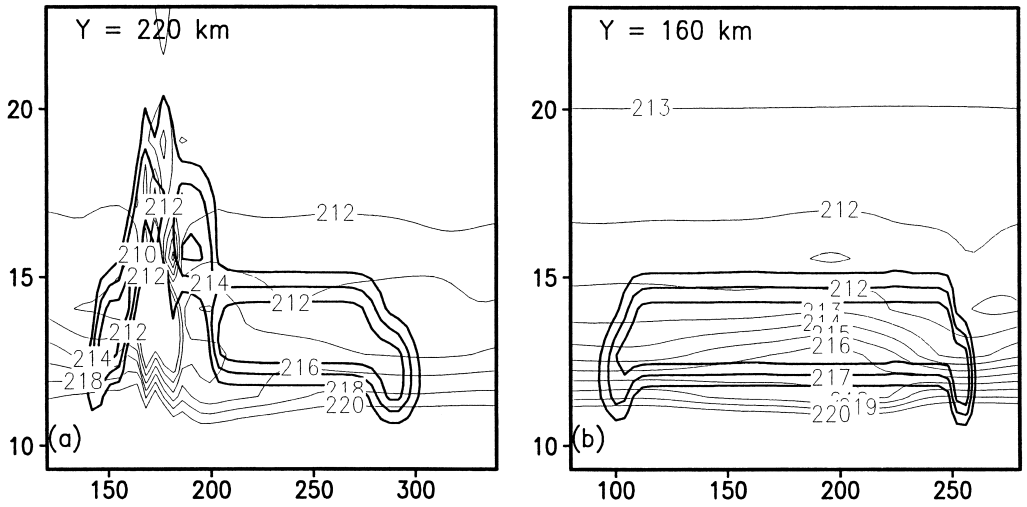

FIG. 2. Vertical cross sections of the 10.7-μm weighting function (m^{-1}; multiplied by 10^5; thick contours) along with RAMS predicted temperatures (K; thin contours) at (a) y = 220 km and (b) y = 160 km. These locations are also indicated as dotted contours in Fig. 1a.

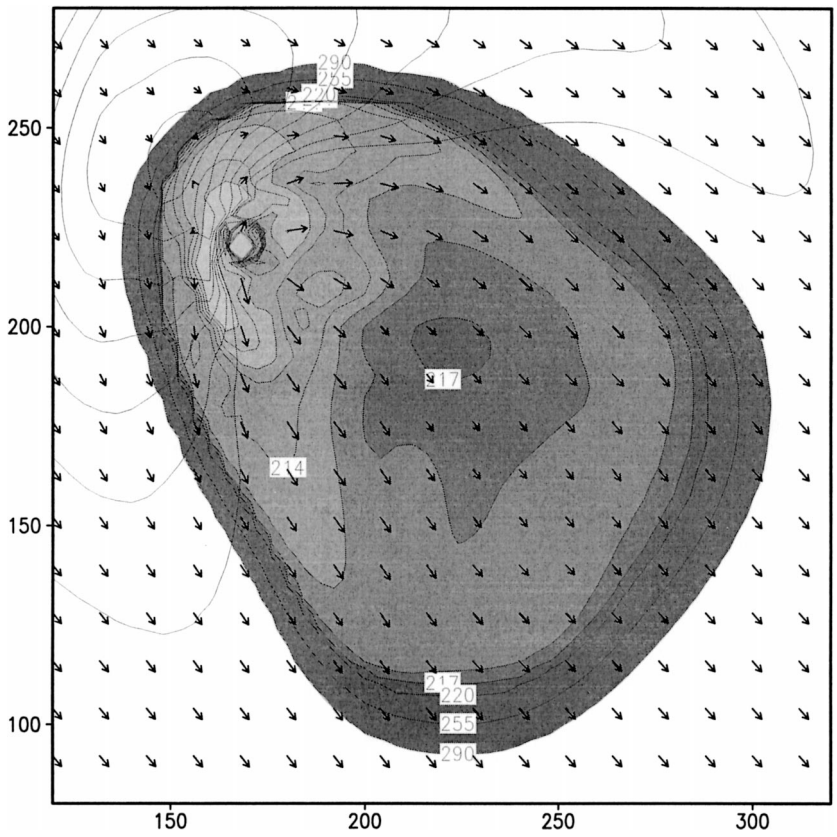

FIG. 3. Shaded and contoured values of 10.7-μm T_bs (K) along with ground-relative horizontal wind vectors at anvil level. In addition, π^* is contoured and shows the location of the upstream region of high pressure that also flanked the anvil on the left and right sides.

fields were superimposed on the T_b field (Fig. 3). Both fields were chosen at a height (approximately 12.8 km) where the total condensate field occupied nearly the same area as that bounded by the 290-K T_b contour. Aside from the enhanced V, other noteworthy features typical of some thunderstorms are the region of high pressure (located near $x = 150$ and $y = 240$ km) and the horizontally divergent wind field about the overshooting dome. The V or U shape of the cooler T_bs is also characteristic of both the wind and pressure fields. Maximum values of the perturbation Exner function curve occur about the rear, left, and right flanks of the anvil. Similarly, the wind field within the enhanced V suggests that streamlines resemble curved segments of the letter U. If we superimpose on the shaded T_b field only those wind vectors whose magnitude is at least 30 m s^{-1}, the region occupied by these vectors is shaped like the letter U (see Fig. 4a). This implies the existence of two localized jets that emanate from the overshooting dome.

A plot of the streamlines (Fig. 4b) also shows that the flow originates from the overshooting dome. Streamlines to the northwest of the overshooting dome encounter southeasterly oriented streamlines of the environment, demarking a stagnation point. From the stagnation point, streamlines curve around the left and right flanks of the anvil, like the letter U.

Results also suggest that the enhanced V may form in response not only to dynamical factors but also from interaction between the thunderstorm and environment. A general property of overshooting domes is that rising air within the overshooting dome is approximately 10 K cooler than the environment, as in this case. Because of mass flux into the dome, a localized region of high pressure forms at the overshooting top. Mass continuity dictates that air should accelerate away horizontally from the dome at a level higher (hence colder) than the main body of the anvil. Consequently, T_bs of the region near and containing the overshooting dome are colder compared to those of the anvil (Fig. 3). Alternatively, the T_b field in Fig. 3 may be viewed as a topographical map. The region downwind of the overshooting dome contains sinking motion on the order of a few centimeters per second, which moves air to lower (hence warmer) levels. Further, the high pressure field that flanks the rear of the anvil causes air that originated from the overshooting dome to decelerate. Next, air turns away from the stagnation point while the flanking

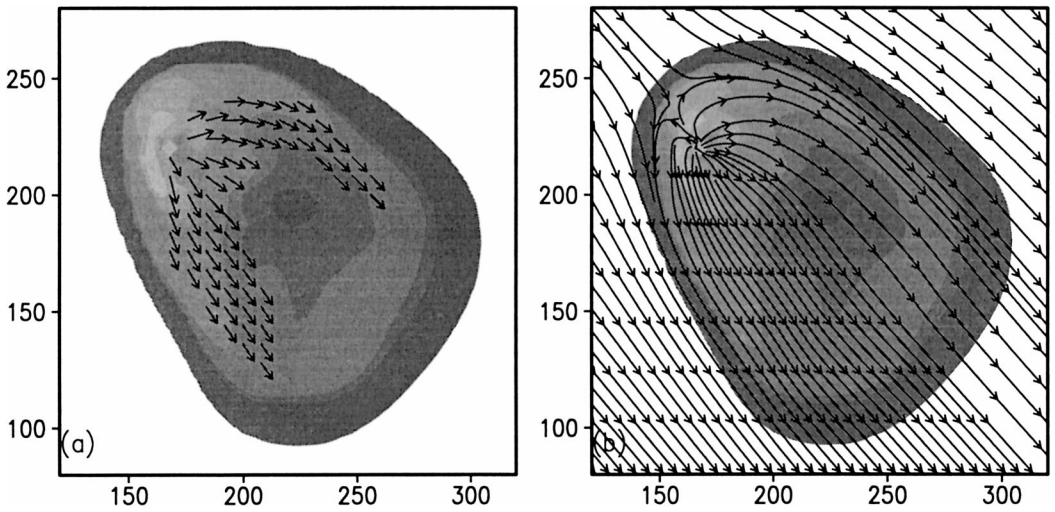

FIG. 4. Shaded values of 10.7-μm T_bs (K) along with (a) ground-relative horizontal wind vectors whose magnitude was at least 30 m s^{-1} and (b) ground-relative streamlines.

high accelerates air along the right and left flanks of the anvil. That is, the flanking high pressure region gives rise to curved streamlines that emanate from the rear flank of the overshooting dome (Fig. 4b). Furthermore, the flanking region of high pressure decelerates and turns the environmental flow near the stagnation point around the right and left flanks of the anvil.

In short, three regions of curved flow are identified that exist within the enhanced V: 1) a localized jet flow; 2) northwestward air movement away from the overshooting dome that turns while accelerating along the right and left flanks of the anvil; and 3) environmental air turned by the flanking region of high pressure. These results imply that the enhanced V formed in response to advection of elevated and cooler cloud material that subsequently sank and warmed with these three regions of curved flow. In particular, the legs of the enhanced V along the right and left flanks of the anvil formed from the two localized jet flows seen in Fig. 4a.

4. Microphysical quantities and brightness temperatures

Simulations offer an opportunity to examine the relationships between microphysical and T_b fields. Such relationships have application to remote sensing and may also determine the potential information content of 10.7-μm measurements in data assimilation. Comparisons will focus on pristine ice and rainwater since it was shown earlier that the computed T_b field can essentially be reproduced by considering only pristine ice. Rainwater, on the other hand, was chosen because of interest in inferring surface rain rates from satellite infrared data.

The relationship between 10.7-μm T_b and CIRp has several interesting and distinct features (Fig. 5a). Three regions may be identified: an optically thick region (greater than 5), a transition region (0.1–5), and an ultra optically thin region (less then 0.1). As expected, the ultra optically thin region exhibits no relationship between T_b and CIRp owing to the large contribution from surface emission. We should stress, however, that such clouds are not detectable by current satellite measurement systems. A strong negative correlation exists in the transition region, that is, for optically thin portions of the thunderstorm anvil. This is a result of the close relationship between T_b and optical depth (see inset in Fig. 5a). In optically thick areas of the anvil there is little if any relationship as a result of the saturation of brightness temperatures as a function of optical depth.

In contrast, a plot of T_b against CIRr (Fig. 5b) vaguely resembles that of CIRp in that there are also similar identifiable regimes; however, the relationship is much more dispersive. This is especially true in the transition region where CIRr may vary by two orders of magnitude or more for a given T_b. Note that other hydrometeors produced similar relationships (results not shown), some of which had slightly less dispersion. However, even in these cases the relationships did not approach the high correlation seen for pristine ice. At the coldest T_bs (less then 220 K) there is virtually no relationship between 10.7-μm T_bs and CIRr.

Also of interest is the correlation of mean particle diameter with T_b. The effective mean diameter field for pristine ice is shown in Fig. 6, indicating surprising variation in the optically thickest parts of the anvil. When T_bs are correlated with EFFDRp there are also three distinct regions that emerge (Fig. 7a). But in this case the transition region has a positive correlation, im-

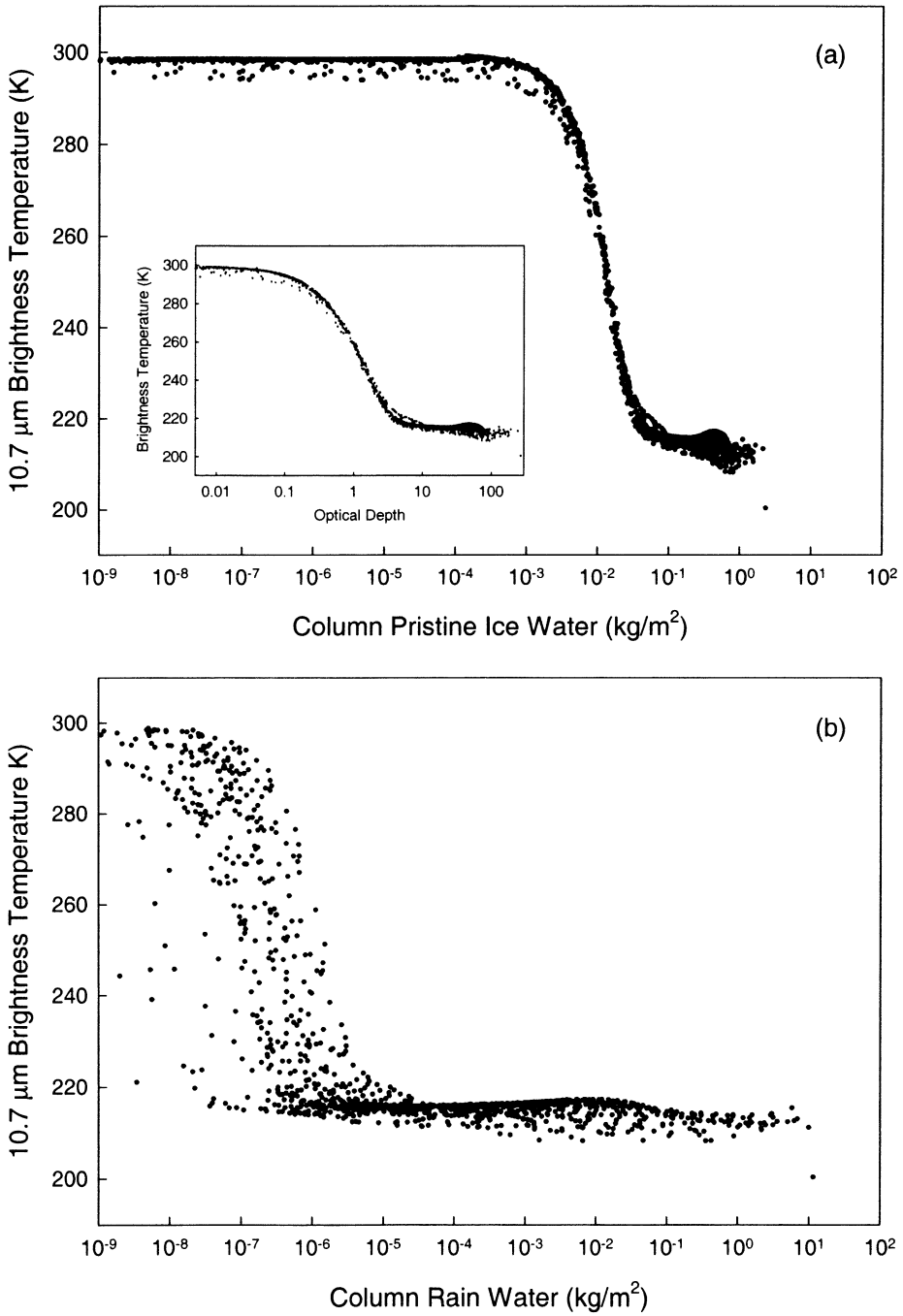

FIG. 5. Scatterplot of 10.7-μm T_bs with column-integrated (a) pristine ice mass (optical depth for inset) and (b) rainwater mass (kg m^{-2}).

plying that particle size increases with decreasing CIRp in this region. This presumably is caused by the fact that number concentration in this region falls off faster than cloud mixing ratio [recall that mean particle size is proportional to $(r_c/N_c)^{1/\beta}$]. Particle sizes range mainly from 20 to 80 μm. The largest particles (greater than 100 μm) appear to occur at the anvil edges, but are in very low number concentrations. Again, at the coldest temperatures there is no correlation between T_b and particle size.

In contrast to pristine ice, the relationship of T_b to EFFDRr is confined to T_bs less than 220 K (Fig. 7b). As before, there is no relationship between the two quantities. Further analysis in the form of horizontal

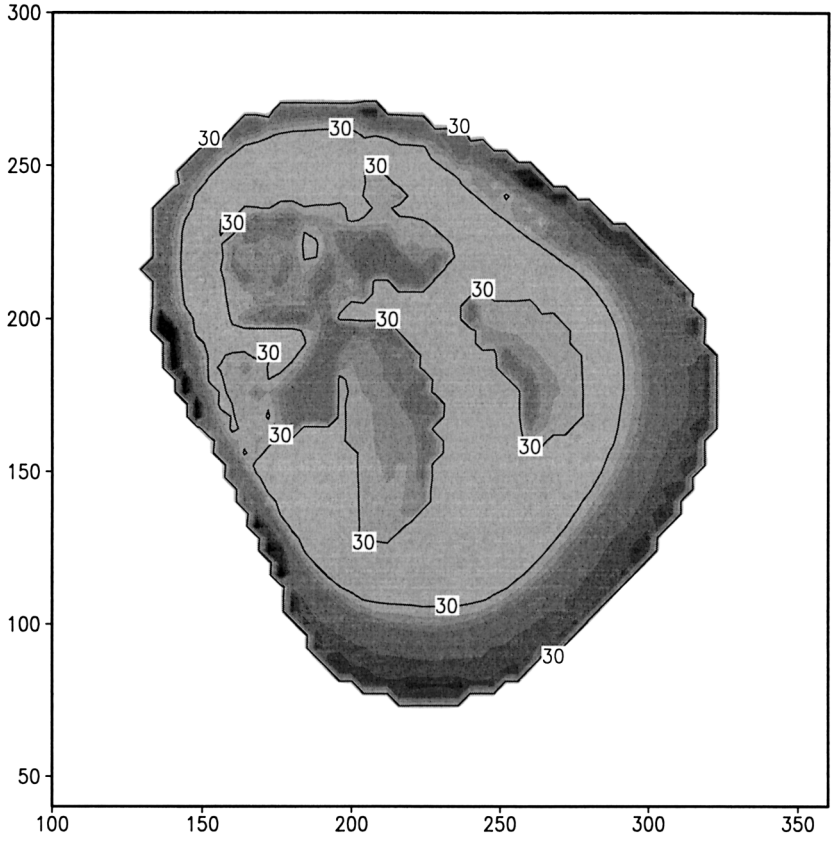

FIG. 6. Shaded and contoured values of effective mean diameter for pristine ice (μm).

fields of T_b, total water condensate, and surface precipitation rate (see Fig. 8) illustrates that both quantities occur within a relatively narrow range of T_bs. The general trend that one sees from these results is that the relationships are similar for all hydrometeors with larger fall speeds, that is, rain, graupel, and hail. Hydrometeors with relatively small fall speeds, that is, pristine ice, snow, and aggregates, have similar relationships as well, but tend to show somewhat greater correlation between T_b and microphysics. In short, particles with larger fall speeds tend to appear in lower portions of the cloud, thereby effectively decoupling them from the outgoing radiance field.

5. Conclusions and future development

Analysis of 10.7-μm T_bs computed for a simulated severe thunderstorm using a sophisticated microphysical scheme has yielded further insight into the cause of the enhanced V and the interaction between infrared radiation and storm microphysics. Results suggested that the enhanced V was produced by the interaction between the overshooting dome and the region of high pressure located upstream. In short, the enhanced V was created by downstream and subsiding transport of relatively cold cloud material ejected from the overshooting dome. The classic V shape was caused not only by the two localized jets originating from the overshooting dome, but also the reorientation of the flow by the upstream high. This interpretation is contrary to one in which the overshooting dome is considered merely as an obstacle to the flow. Not surprisingly, the cloudy 10.7-μm T_b field was found to be almost exclusively a result of the radiative effects of the anvil, which was composed mainly of pristine ice particles. These particles typically varied between 20 and 80 μm in diameter. Also, pristine ice microphysical properties (whether mass or size) played little or no role in determining the T_b field except in those areas of the anvil with optical depths less than about 5. The implication is that for optically thin portions of the anvil there is available information about the integrated water content of the anvil at 10.7 μm and somewhat less information concerning particle size. In contrast, 10.7-μm T_bs showed virtually no correspondence with either large hydrometeors, such as rainwater or surface precipitation rate. While results were only obtained with one snapshot of a single case, we anticipate similar relationships will exist for other deep convective systems at similar stages in their development.

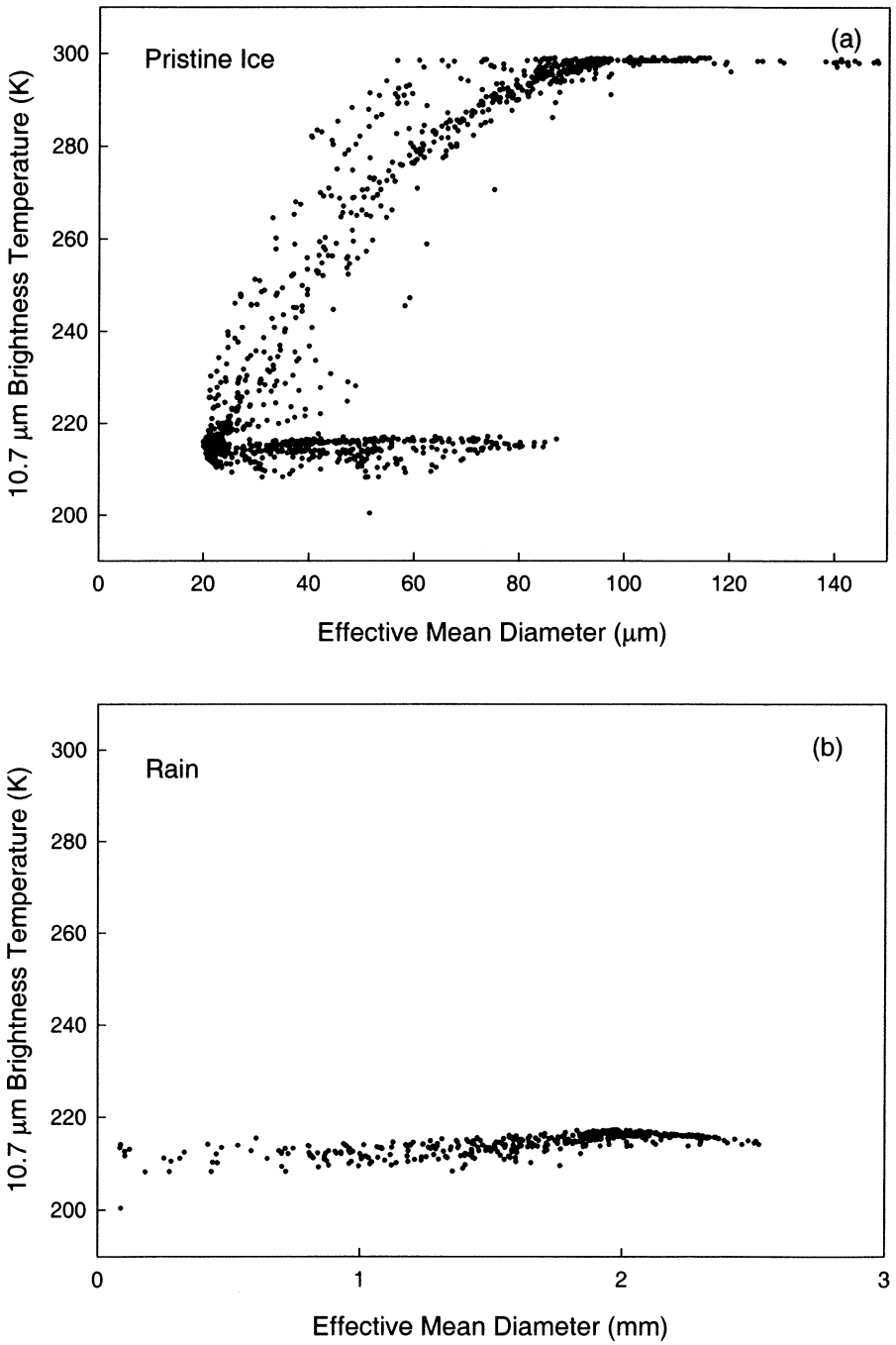

FIG. 7. Scatterplot of 10.7-μm T_bs with effective mean diameter (μm) of (a) pristine ice and (b) rainwater (mm).

The modeling system utilized in this study has further application in satellite product development, information content studies, and satellite data assimilation. For instance, developing severe weather and tropical cyclone products well in advance of the launch of a satellite can effectively extend the operational use of a sensor. Data assimilation is perhaps the most significant application given the inability of current operational weather forecast models to fully utilize satellite data in cloudy regions. Satellite observations that provide the greatest potential are those at microwave wavelengths. These observations would provide far more information on hydrometeor vertical structure and microphysical characteristics. The observational operator utilized here

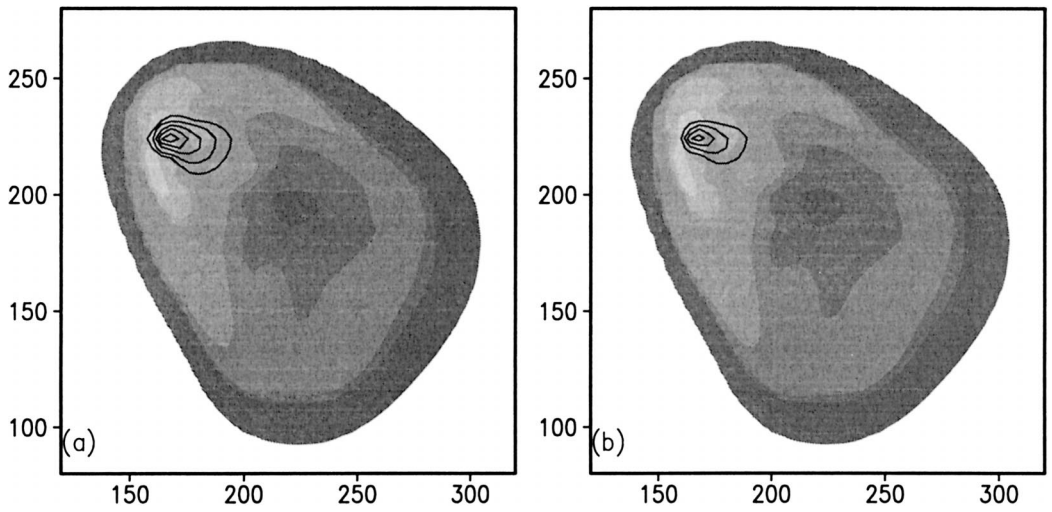

FIG. 8. Shaded values of 10.7-μm T_bs (K) along with contoured values of (a) total surface condensate (0.2, 0.5, 1.0, 1.5, and 2.0 g kg^{-1}) and (b) surface precipitation rate (20, 40, 60, and 80 mm h^{-1}).

may be easily adapted to these wavelengths by including an appropriate gas extinction model. This is reserved as a topic of future work.

Acknowledgments. This material is based on work supported by the National Oceanic and Atmospheric Administration under Grant NA67RJ0152 and DoD Center for Geosciences/Atmospheric Research Grant DAAL01-98-2-0078. Thanks are extended to not only David Mitchell for ADT code and suggestions, but also Drs. Tristan L'Ecuyer and Stan Kidder for their suggestions.

REFERENCES

Adler, R. F., and D. D. Fenn, 1979: Thunderstorm intensity as determined from satellite data. *J. Appl. Meteor.*, **18,** 502–517.

——, M. J. Markus, D. D. Fenn, G. Szejwach, and W. E. Shenk, 1983: Thunderstorm top structure observed by aircraft overflights with an infrared radiometer. *J. Climate Appl. Meteor.*, **22,** 579–593.

Arakawa, A., and V. Lamb, 1981: A potential enstrophy and energy conserving scheme for the shallow water equations. *Mon. Wea. Rev.,* **109,** 18–36.

Chevallier, F., and G. Kelly, 2002: Model clouds as seen from space: Comparison with geostationary imagery in the 11-μm window channel. *Mon. Wea. Rev.*, **130,** 712–722.

——, P. Bauer, G. Kelly, C. Jakob, and T. McNally, 2001: Model clouds over oceans as seen from space: Comparison with HIRS/2 and MSU radiances. *J. Climate,* **14,** 4216–4229.

Deeter, M., and K. F. Evans, 1998: A hybrid Eddington–single scatter radiative transfer model for computing radiances from thermally emitting atmospheres. *J. Quant. Spectrosc. Radiat. Transfer,* **60,** 635–648.

Downing, H. D., and D. Williams, 1975: Optical constants of water in the infrared. *J. Geophys. Res.,* **80,** 1656–1661.

Evans, K. F., 1998: The spherical harmonics discrete ordinate method for three-dimensional atmospheric radiation transfer. *J. Atmos. Sci.,* **55,** 429–446.

Grasso, L. D., 2000: The dissipation of a left moving cell in a severe storm environment. *Mon. Wea. Rev.,* **128,** 2797–2815.

Greenwald, T. J., R. Hertenstein, and T. Vukicevic, 2002: An all-weather observational operator for radiance data assimilation with mesoscale forecast models. *Mon. Wea. Rev.,* **130,** 1882–1897.

Heymsfield, G. M., and R. H. Blackmer, 1988: Satellite-observed characteristics of Midwest severe thunderstorm anvils. *Mon. Wea. Rev.*, **116,** 2200–2224.

Huffman, G. J., and Coauthors, 1997: The Global Precipitation Climatology Project (GPCP) combined precipitation dataset. *Bull. Amer. Meteor. Soc.*, **78,** 5–20.

Klemp, J. B., and R. B. Wilhelmson, 1978: The simulation of three-dimensional convective storm dynamics. *J. Atmos. Sci.,* **35,** 1070–1096.

Lilly, D. K., 1962: On the numerical simulation of buoyant convection. *Tellus,* **14,** 148–172.

Liou, K., 1980: *An Introduction to Atmospheric Radiation.* Academic Press, 392 pp.

McCann, D. W., 1983: The enhanced-V: A satellite observable severe storm signature. *Mon. Wea. Rev.,* **111,** 887–894.

McMillin, L. M., L. J. Crone, M. D. Goldberg, and T. J. Kleespies, 1995a: Atmospheric transmittance of an absorbing gas, 4. OPTRAN: A computationally fast and accurate transmittance model for absorbing gases with fixed and variable mixing ratios at variable viewing angles. *Appl. Opt.,* **34,** 6269–6274.

——, ——, and T. J. Kleespies, 1995b: Atmospheric transmittance of an absorbing gas, 5. Improvements to the OPTRAN approach. *Appl. Opt.,* **34,** 8396–8399.

Meyers, M. P., R. L. Walko, J. Y. Harrington, and W. R. Cotton, 1997: New RAMS cloud microphysics parameterization. Part II: The two-moment scheme. *Atmos. Res.,* **45,** 3–39.

Mitchell, D. L., 1996: Use of mass- and area-dimensional power laws for determining precipitation particle terminal velocities. *J. Atmos. Sci.,* **53,** 1710–1723.

——, 2000: Parameterization of the Mie extinction and absorption coefficients for water clouds. *J. Atmos. Sci.,* **57,** 1311–1326.

——, 2002: Effective diameter in radiation transfer: General definitions, applications, and limitations. *J. Atmos. Sci.,* **59,** 2330–2346.

——, and W. P. Arnott, 1994: A model predicting the evolution of ice particle size spectra and radiative properties of cirrus clouds. Part II: Dependence of absorption and extinction on ice crystal morphology. *J. Atmos. Sci.,* **51,** 817–832.

Pielke, R. A., and Coauthors, 1992: A comprehensive meteorological modeling system—RAMS. *Meteor. Atmos. Phys.,* **49,** 69–91.

Smagorinsky, J., 1963: General circulation experiments with the

primitive equations. Part I. The basic experiment. *Mon. Wea. Rev.*, **91,** 99–164.

Tripoli, G. J., and W. R. Cotton, 1981: The use of ice-liquid water potential temperature as a thermodynamic variable in deep atmospheric models. *Mon. Wea. Rev.*, **109,** 1094–1102.

——, and ——, 1982: The Colorado State University three dimensional cloud mesoscale model, 1982. Part I: General theoretical framework and sensitivity experiments. *J. Rech. Atmos.*, **16,** 185–220.

Vicente, G. A., R. A. Scofield, and W. P. Menzel, 1998: The operational GOES infrared rainfall estimation technique. *Bull. Amer. Meteor. Soc.*, **79,** 1883–1898.

Warren, S. G., 1984: Optical constants of ice from the ultraviolet to the microwave. *Appl. Opt.*, **23,** 1206–1225.